

# Combining Local Filtering and Multiscale Analysis for Edge, Ridge, and Curvilinear Objects Detection

Sylvain Berlemont, *Student Member, IEEE*, and Jean-Christophe Olivo-Marin, *Senior Member, IEEE*

**Abstract**—This paper presents a general method for detecting curvilinear structures, like filaments or edges, in noisy images. This method relies on a novel technique, the feature-adapted beamlet transform (FABT) which is the main contribution of this paper. It combines the well-known Beamlet transform (BT), introduced by Donoho *et al.*, with local filtering techniques in order to improve both detection performance and accuracy of the BT. Moreover, as the desired feature detector is chosen to belong to the class of steerable filters, our transform requires only  $O(N \log(N))$  operations, where  $N = n^2$  is the number of pixels. Besides providing a fast implementation of the FABT on discrete grids, we present a statistically controlled method for curvilinear objects detection. To extract significant objects, we propose an algorithm in four steps: 1) compute the FABT, 2) normalize beamlet coefficients, 3) select meaningful beamlets thanks to a fast energy-based minimization, and 4) link beamlets together in order to get a list of objects. We present an evaluation on both synthetic and real data, and demonstrate substantial improvements of our method over classical feature detectors.

**Index Terms**—Beamlet transform, curvilinear objects, edge, feature, Radon transform, ridge, statistical detection, steerable filters.

## I. INTRODUCTION

THE problem of detecting curvilinear objects in images arises in various areas of image processing and computer vision since such kind of objects occur in every natural and synthetic images, like roads and streams in remote sensing images, human vasculature in medical imaging, or filamentary structures in biological microscopy. Edges can be also perceived as curvilinear objects since they describe discontinuities along curves [11]. Therefore, detection of such features is probably one of the most important step toward object recognition and shape analysis.

Commonly, curvilinear objects are considered as 1-D manifolds that have a specific transverse profile running along a smooth curve. The shape of this profile may be an edge- or a ridge-like feature. It can also be represented by more complex

Manuscript received August 27, 2008; revised July 21, 2009. This work was supported in part by Genomic Vision S.A. and A.N.R.T. First published August 25, 2009; current version published December 16, 2009. The associate editor coordinating the review of this manuscript and approving it for publication was Dr. Thomas S. Denney.

S. Berlemont was with the Institut Pasteur, Quantitative Image Analysis Unit, CNRS URA 2582, 75015 Paris, France. He is now with the Cell Biology Department, Harvard Medical School, MA 02115 Boston USA (e-mail: sylvain\_berlemont@hms.harvard.edu).

J.-C. Olivo-Marin is with the Institut Pasteur, Quantitative Image Analysis Unit, CNRS URA 2582, 75015 Paris, France (e-mail: jcolivo@pasteur.fr).

Color versions of one or more of the figures in this paper are available online at <http://ieeexplore.ieee.org>.

Digital Object Identifier 10.1109/TIP.2009.2030968

designed features. In the context of biological imaging, the diameter of structures such as microtubules or DNA molecules for instance is about 3 nm, which is far smaller than the point spread function (PSF) width of any standard microscope. Hence, it is acceptable to consider the transverse profile of such filaments to be approximated by a PSF model [46].

One way to detect curvilinear objects is to track locally the feature of the line profile; linear filtering or template matched filtering are well-known techniques for doing so. The classical Canny edge detector [14] is based on such linear filtering techniques. It involves the computation of correlations with shifted and/or rotated version of the feature template at every point in the image. Filtering is usually followed by a nonmaxima suppression and a thresholding step. These two processes yield a set of pixels which have to be linked together with a contour tracing algorithm. This final step may be tedious and has a high complexity [16].

Recently, optimized detectors have been proposed [35] that out-perform classical feature detectors like Canny edge detector or Hessian-based filter for ridge detection [25]. Authors define a general approach for the design of 2-D feature detectors from a class of steerable filters [27]. In this framework, a convolution of an image with a steerable filter of arbitrary orientation is equal to a finite weighted sum of convolutions of the same image with a limited number of basis filters, which are independent of the filter's orientation. They consider an  $M$ th-order detector of the form

$$h(x, y) = \sum_{k=1}^M \sum_{i=0}^k \alpha_{k,i} \frac{\partial^{k-i}}{\partial x^{k-i}} \frac{\partial^i}{\partial y^i} g(x, y) \quad (1)$$

where  $g(x, y)$  is a Gaussian function. The  $\alpha_{k,i}$ 's are obtained by optimization of a Canny-like criterion. Due to the steerable ability of such filters, the authors derive the filter's orientation that gives the highest response by solving an  $M$ th-order polynomial equation at every point in the image. This technique yields to a significant performance improvement over classical approaches, without any relevant computational time increase. The major drawbacks of the above approaches come from the fact that linear filtering is based on local operators: it is highly sensitive to noise but not sensitive to the underlying smoothness of the curve, which is a typical nonlocal property of curvilinear objects.

Alternatively, line detection can be performed with the Radon transform. Also known as the Hough transform in the case of discrete binary images, it performs a mapping from the image space into a line parameter space by computing line integrals. Formally, the continuous Radon transform of a 2-D image  $f$ ,

denoted as  $\mathcal{R}[f](\theta, \rho)$ , is defined as the line integral of  $f$  along a line oriented along an angle  $\theta$  and at distance  $\rho$  from the origin

$$\mathcal{R}[f](\theta, \rho) = \int \int f(x, y) \delta(x \cos(\theta) + y \sin(\theta) - \rho) dx dy. \quad (2)$$

Peaks in the parameter space reveal potential lines of interest. This is a very reliable method for detecting bright lines in noisy images. However, there are several limitations. First this transform cannot be used to detect lines carrying a specific line profile for it only integrates image intensity along thin lines; it cannot make any difference for instance between a line passing over a real linear structures and a line passing through a bright spot. Moreover, Radon transform computes line integrals on full lines that pass through the whole image domain and does not take into account shorter segments.

Direct evaluation of line integrals on the complete set of all segments in a given image is computationally untrackable. Indeed, given an image of  $N = n \times n$  pixels, the number of possible line segments defined is in  $O(N^2)$ . One of the methodologies proposed to address this problem is the Beamlet transform [22], [23]. This transform belongs to the multiscale analysis family which aims at describing the image, or some components therein, as an atomic decomposition into a given basis [40]. Wavelet transform [17], [37], ridgelet transform [10], [19] and curvelet transform [11] are well-known multiscale analysis tools used in image approximation [12], [13], image compression [18], blind source separation [8] or image restoration [41], [45]. Several directionally adaptive transforms (bandeleets [36], contourlets [20], directionlets [43]) derived from multiscale analysis have been proposed recently to optimally represent images containing multidirectional structures. These transforms have been applied successfully to data compression, texture analysis and denoising. For detection purposes, Beamlet transform has shown good performances for segments and curves extraction [1], [24], [30], [33], [42]. It defines a set of dyadically organized line segments occupying a range of dyadic locations and scales, and spanning a full range of orientations. This system of line segments, called beamlets, have both their end-points lying on dyadic squares that are obtained by recursive partitioning of the image domain (see [23] for complete details). The collection of beamlets has a  $O(N \log(N))$  cardinality. The underlying idea of the Beamlet transform is to compute line integrals only on this smaller set, which is an efficient substitute of the entire set of segments for it can approximate any segment by a finite chain of beamlets. Thereafter, beamlet chaining technique provides a reliable way to approximate segments or any piecewise constant curves [2], [31], [32], [34]. Beamlet transform can be viewed as a multiscale Radon transform: they both integrate image intensity along line segments. As they cannot take into account line profile, edge- or ridge-like feature for instance, they are not well-adapted to detect curvilinear objects carrying a specific line profile.

The main contribution of this paper is to propose a method for doing so. It combines the Beamlet transform with local filtering technique in order to introduce what we call the feature-adapted beamlet transform (FABT). This approach proposes a general way to efficiently incorporate line profiles, such as edge- or

ridge-like feature, into Radon and Beamlet transforms. FABT will be presented in Section II and a fast implementation on discrete grids will be provided. Section III presents a FABT-based fully automated detection method of curvilinear objects such as contours or filaments, with a statistical control over false positives. Section IV proposes experiments on synthetic data demonstrating substantial improvements of the FABT over the classical Beamlet transform. These improvements concern both good detection performance and angular accuracy. We also present some edge and ridge detection results on real data images. Section V concludes the paper.

## II. FEATURE-ADAPTED BEAMLET TRANSFORM

The main contribution of this paper is to propose a general way to incorporate any line profile, such as edge or ridge feature, into the Beamlet transform. This is done by integrating these profile into Radon lines, for it is the internal tool used to compute such transform.

### A. Continuous Feature-Adapted Radon Transform

Let  $f$  be an image defined on a sub-space of  $\mathbb{R}^2$  and let  $h$  be a feature detector designed to filter specifically a 2-D line profile, for instance, an edge, a ridge or a more complex image feature. For detection purposes, this filter should have the ability to detect the feature for which it has been designed whatever the level of background intensity. Hence,  $h$  should be a band-pass filter of null mean

$$\int \int h(x, y) dx dy = 0. \quad (3)$$

Let  $h^\theta$  be a rotated version of  $h$  along the direction  $\theta$

$$h^\theta(x, y) = h(\mathbf{R}_\theta(x, y)) \quad (4)$$

where  $\mathbf{R}_\theta$  is the 2-D rotation matrix of angle  $\theta$ . In a first step, we filter the image  $f$  with  $h^\theta$  before computing a Radon coefficient thanks to (2). This filtering step will enhance structures oriented at an angle  $\theta$  and carrying the specific line profile, while getting rid of other structures in the image. For any distance  $\rho$  from the origin, we have

$$\begin{aligned} & \mathcal{R}[f * h^\theta](\theta, \rho) \\ &= \int \int f * h^\theta(x, y) \delta(x \cos(\theta) + y \sin(\theta) - \rho) dx dy. \end{aligned} \quad (5)$$

A high coefficient means that the local feature oriented at an angle  $\theta$  runs significantly along the line  $(\theta, \rho)$ . We call (5) the feature-adapted Radon transform. In general, the computation of all these coefficients is not conceivable, since it requires to convolve the image as many times as the number of  $\theta$ 's. For the special case where  $h$  is selected to be within the class of steerable filters [27], we can write  $h^\theta$  as a linear combination of basis filters

$$h^\theta(x, y) = \sum_{i=1}^M \phi_i(\theta) h^{\theta_i}(x, y) \quad (6)$$

where  $\phi_i$ 's are interpolation functions that only depend on  $\theta$  and the basis filters  $h^{\theta_i}$ 's are independent of  $\theta$ . A convolution of an

image with a steerable filter of arbitrary orientation is equal to a finite weighted sum of convolution of the same image with the basis filters. As a result

$$\begin{aligned}
& \mathcal{R}[f * h^\theta](\theta, \rho) \\
&= \int \int f * \sum_{i=1}^M \phi_i(\theta) h^{\theta_i}(x, y) \delta(x \cos(\theta) + y \sin(\theta) - \rho) dx dy \\
&= \sum_{i=1}^M \phi_i(\theta) \int \int f * h^{\theta_i}(x, y) \delta(x \cos(\theta) + y \sin(\theta) - \rho) dx dy \\
&= \sum_{i=1}^M \phi_i(\theta) \mathcal{R}[f * h^{\theta_i}](\theta, \rho). \tag{7}
\end{aligned}$$

Thanks to this result, (5) reduces to a linear combination of classical Radon transforms applied on filtered version of image  $f$ . In the next section, we will see how to implement this scheme on discrete grids.

### B. Implementation on Discrete Grids

1) *Discrete Radon Transform*: Much attention has been given over the last twenty years to adapt the classical Radon transform to digital arrays, i.e., when  $f$  is represented by a discrete array  $I = I(u, v) : -n/2 \leq u, v < n/2$ . Intuitively, if we consider the number of Radon coefficients to be of the same order as the number of pixels of the image, a straightforward implementation requires  $O(N^2)$  operations. This complexity is not conceivable for practical applications. Recently, a novel Fourier-based approach has been proposed in order to compute the discrete Radon transform [4] in a fast and accurate way. The method relies on a discrete Fourier slice theorem, which associates the discrete Radon transform with the pseudo-polar Fourier transform. The algorithm is fast since it computes the 2-D discrete Radon transform using  $O(N \log N)$  operations, where  $N = n^2$  is the number of pixels in the image. According to this methodology, a *basically horizontal* line is a line of the form  $y = \tan(\theta)x + t$ , where  $t \in \mathbb{R}$  is the intercept value on  $y$ -axis and the slope  $|\tan(\theta)| \leq 1$  (In the following, complementary set of *basically vertical* lines of form  $x = \tan(\theta)y + t$  is treated identically). The discrete Radon transform associated with such line set is defined as

$$\mathcal{R}[I](\theta, t) = \sum_u \tilde{I}(u, \tan(\theta)u + t) \tag{8}$$

where  $\tilde{I}(u, y)$  is an interpolant, that takes discrete values in the first argument and continuous values in the second argument. The 1-D interpolation is realized thanks to a Dirichlet kernel (see [4] for complete details). The parameterization of the Radon space is chosen as follows: one considers only the lines having an intercept  $-n \leq t < n$  and the set of angles  $\theta = \arctan(2l/n)$ ,  $-n/2 \leq l < n/2$ . According to this set of angles, the fundamental property of (8) is driven by the following result:

*Theorem 1 (Projection-Slice Theorem)*: Define the 2-D Fourier transform of the array  $I$  via

$$\hat{I}(k_1, k_2) = \sum_{u,v} I(u, v) \exp \left\{ -i \frac{\pi}{n} (uk_1 + vk_2) \right\}$$

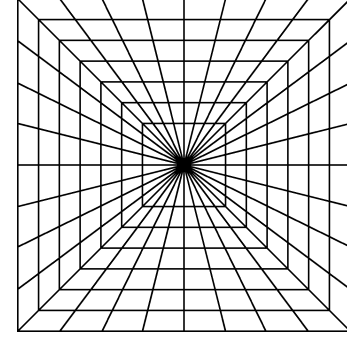


Fig. 1. Pseudo-polar grid for  $n = 8$ .

where  $-n \leq k_1, k_2 \leq n$ . Then, for each fixed  $\theta = \arctan(2l/n)$ ,  $-n/2 \leq l < n/2$ , the  $2n$  numbers

$$\mathcal{R}[I](\theta, t), \quad -n \leq t < n$$

are a 1-D discrete Fourier transform pair with the  $2n$  numbers

$$\hat{I}\left(\pi \frac{k}{n} \tan(\theta), \pi \frac{k}{n}\right), \quad -n \leq k < n.$$

The key point of this theorem relies on the special nature of the angles  $\theta$  chosen above. Using Theorem 1, one has a connection between Radon values and a set of spatial frequencies  $\xi_{l,k} = (\pi(k/n)(2l/n), \pi k/n)$  with  $-n \leq k < n$  and  $-n/2 \leq l < n/2$ . This is a special non-Cartesian point set in frequency domain which has been known as the pseudo-polar grid, and is depicted in Fig. 1.

This point set can be efficiently computed according to the pseudo-polar fast Fourier transform [3], noted  $\mathcal{P}$ .  $\mathcal{P}[I]$  is an array of  $2n$  rows by  $n$  columns where the  $l$ th column refers to the values  $\hat{I}(\pi(k/n)(2l/n), \pi k/n)$ ,  $-n \leq k < n$ . Hence, thanks to Theorem 1, the discrete Radon transform of (8) is reduced to  $\mathcal{R} = \mathcal{F}_{-1} \circ \mathcal{P}$ , where  $\mathcal{F}_{-1}$  denotes the 1-D inverse Fourier transform performed on each column of  $\mathcal{P}[I]$ . In that methodology, the number of Radon coefficients is  $4N$  ( $2N$  for basically horizontal lines and  $2N$  for basically vertical lines).

2) *Discrete Feature-Adapted Radon Transform*: We choose the methodology described above to implement the Feature-adapted Radon transform on discrete grids. Using the discrete definition introduced in previous paragraph, we rewrite (5) as

$$\mathcal{R}[I * h^\theta](\theta, t) = \sum_u \widetilde{I * h^\theta}(u, \tan(\theta)u + t). \tag{9}$$

We state the following result.

*Proposition 1*: For each fixed  $\theta = \arctan(2l/n)$ ,  $-n/2 \leq l < n/2$ , the  $2n$  numbers

$$\mathcal{R}[I * h^\theta](\theta, t), \quad -n \leq t < n$$

are a 1-D discrete Fourier transform pair with the  $2n$  numbers

$$\sum_{i=1}^M \phi_i(\theta) \widehat{I * h^{\theta_i}}\left(\pi \frac{k}{n} \tan(\theta), \pi \frac{k}{n}\right), \quad -n \leq k < n.$$

The proof is given in Appendix A. Thanks to this result, we compute (9) for every angle, as follows: we first convolve the image as many times as the number of basis filters composing

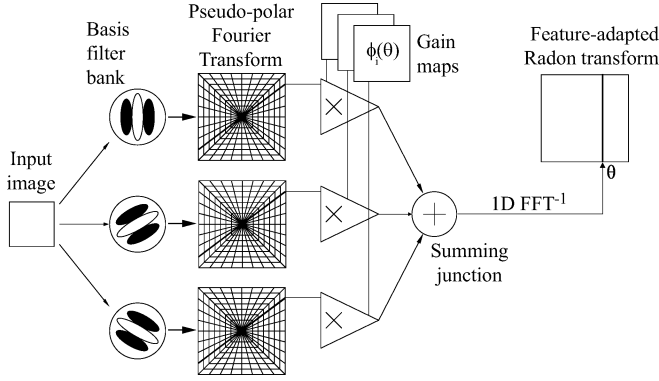


Fig. 2. Feature-adapted Radon transform diagram.

our filter  $h$ . This number is typically very small ( $< 10$ ). On each filtered image, we compute the pseudo-polar Fourier transform and then, for each angle  $\theta = \arctan(2l/n)$ , we extract the  $l$ th column of each transform and combine them thanks to Proposition 1. Finally, we perform 1-D inverse Fourier transforms on each resulting series. All these steps can be performed in  $O(N \log(N))$ . A graphical representation of the method is depicted in Fig. 2.

### C. Extension to Feature-Adapted Beamlet Transform

As we have discussed in Section I, Radon transform is not adapted to represent segments since it only gives information on lines passing through the whole image domain. We suggest that Beamlet transform is a good tool to represent segments. In [7], we used a technique akin to the one presented here, in that we embedded a profile that is represented by a steerable filter into the Beamlet transform. A two-scale recursion technique in order to compute beamlet coefficients was used, where beamlets at a given scale can be obtained by the combination of beamlets coefficients computed at smaller scales. While this strategy is quite fast, it introduces a number of numerical approximations, as it has been pointed out in [9]. Besides, we propose that the feature-adapted beamlet transform can be computed thanks to the method presented in paragraph Section II-B2. Notice that the set of orientations implicitly defined by the beamlet set in [23] exactly matches the  $\theta$ 's defined throughout this section. Hence, the Feature-adapted Radon transform can be applied on every dyadic square that partitions the image domain to compute the feature-adapted beamlet transform (FABT). Fig. 3 summarizes the algorithm. Notice that either the set of all scales and the set of all dyadic squares are computed independently. It allows extensive use of grid computation in order to dispatch calculations on multiple processors. The number of beamlet coefficient is exactly  $4n^2 \log(n)$ .

## III. STATISTICALLY CONTROLLED DETECTION OF CURVILINEAR OBJECTS

Feature-adapted beamlet transform has been successfully used in filament detection algorithms [6]. A typical detection process based on such transform can be described as follows:

**Require:**  $I$  is an image of  $n \times n$  pixels, with  $n = 2^J$ .

```

1: for all  $i, 1 \leq i \leq M$  do
2:   compute  $I^{\theta_i} = I * h^{\theta_i}$ 
3: end for
4: for all scales  $j, 0 < j \leq J$  do
5:   for all  $(k_1, k_2), 0 \leq k_1, k_2 < 2^{J-j}$  do
6:     /* Compute pseudo-polar Fourier transforms */
7:     /*  $S$  is a square of size  $2^j$  located at  $(k_1 2^j, k_2 2^j)$  */
8:     /*  $I_S$  is the portion of image  $I$  defined by  $S$  */
9:     for all  $i, 1 \leq i \leq M$  do
10:      compute  $\mathcal{P}[I_S^{\theta_i}]$ 
11:    end for
12:    /* Combine thanks to proposition (1) */
13:    for all  $\theta = \arctan(2l/2^j), -2^{j-1} \leq l < 2^{j-1}$  do
14:      compute  $r(\cdot) = \sum_{i=1}^M \phi_i(\theta) \mathcal{P}[I_S^{\theta_i}](\theta, \cdot)$ 
15:       $\mathcal{R}[I_S * h^\theta](\cdot, \theta) = \mathcal{F}_{-1}[r(\cdot)]$ 
16:    end for
17:  end for
18: end for

```

Fig. 3. Feature-adapted beamlet transform algorithm.

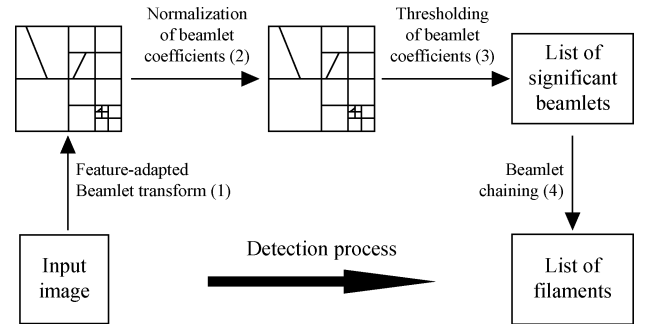


Fig. 4. Workflow of a curvilinear object detection process using feature-adapted beamlet transform.

1) compute the feature-adapted beamlet transform of the image, 2) normalize beamlet coefficients, 3) threshold coefficients, and 4) put beamlets together (chaining) in order to get a list of detected curvilinear objects (filaments, contours, etc.). These steps are depicted in Fig. 4. Despite its robustness, that methodology does not provide real statistical control on the detections and threshold value is usually hard to tune. To satisfy such a statistical demand, we provide here three improvements to our previous work: *i*) a normalization of beamlet coefficients, *ii*) a novel energy-based algorithm to select beamlets, and *iii*) a family of scale-dependent thresholds values on beamlet coefficients. We detail all these improvements below.

### A. Normalization of Coefficients

Our detection method relies on an *a contrario* approach, assuming the image is generated by a noise model only and structures to be detected represent large deviations of such a model. Under the assumption that an image has been generated by a Gaussian noise model, we derive the following result on the distribution of feature-adapted beamlet coefficients.



TABLE I  
SCALE-DEPENDENT THRESHOLD VALUES FOR STATISTICAL  
CONTROL OF BEAMLET COEFFICIENTS

$j$	$\alpha = 10\%$	$\alpha = 1\%$	$\alpha = 0.1\%$
1	2.480	3.226	3.836
2	2.939	3.603	4.164
3	3.345	3.949	4.470
4	3.712	4.269	4.758
5	4.049	4.569	5.031
6	4.362	4.851	5.290
7	4.657	5.119	5.538
8	4.934	5.375	5.776
9	5.198	5.619	6.005
10	5.450	5.854	6.226

Although Radon coefficients are not independent random variables, we choose to approximate the above equation as

$$\prod_{i=1}^{N_j} \mathbb{P}[\tilde{R}[I_S * h^{\theta_i}](\theta_i, t_i) \geq \lambda_j] = \alpha \quad (14)$$

$$\Leftrightarrow \left[ \int_{-\infty}^{\lambda_j} \frac{1}{\sqrt{2\pi}} \exp^{-(1/2)x^2} dx \right]^{N_j} = 1 - \alpha \quad (15)$$

$$\Leftrightarrow \frac{1}{2^{N_j}} \left( 1 + \operatorname{erf}\left(\frac{\sqrt{2}}{2}\lambda_j\right) \right)^{N_j} = 1 - \alpha \quad (16)$$

where  $N_j = 4n_j^2$  is the number of Radon coefficients for a dyadic square of size  $n_j = 2^j$ . We solve this equation for several quantiles  $\alpha = 10\%$ ,  $1\%$ ,  $0.1\%$  in order to exhibit  $\lambda_j$  values for each scale  $0 < j \leq J$ ; Table I gives these values.

#### D. Chaining

This step allows us to obtain the list of curvilinear objects from the list of meaningful beamlets. These segments are independent from each other and need to be linked together in order to obtain the final list of curvilinear objects. In this section, we propose an algorithm to do so. This algorithm proceeds in two steps: first, we chain *basically horizontal* segments on one hand, and the *basically vertical* segments in the other hand. Secondly, we merge these two sets of beamlet chains in order to get the final list of curvilinear structures.

Since the number of beamlet coefficients after thresholding may be quite large, a fast algorithm is needed to perform the chaining. We propose an algorithm that requires  $O(N \log_2(N))$  operations, where  $N$  stands here for the number of beamlets. Fig. 6 depicts the steps for *basically horizontal* segments; same reasoning is applied to the complementary set of basically vertical segments. The procedure consists in traversing the ordered list of segments from the one with the smallest  $x$ -coordinate to the one with the largest  $x$ -coordinate. If a segment which has its left-hand extremity close enough to the right-hand extremity of an already-built beamlet chain, this segment is appended to that chain, otherwise, it is considered as a new chain. In order to search rapidly in the set of chains, which chain is close to a segment, we use a particular tree-based data structures, an associative map [15], to store beamlet chains. This data structure can associate an object, a beamlet chain for instance, to a key of real type, here, the  $y$ -coordinate of the right-hand extremity of the chain. A search of an element into that kind of

**Require:**  $S$  is a set of basically horizontal segments.  $C$  is an associative map.

- 1:  $C \leftarrow \emptyset$
- 2: sort  $S$  according to the  $x$ -coordinate of the left-hand extremity of each segment.
- 3: **for all** segment  $s \in S$  **do**
- 4:  $(x_p, y_p) \leftarrow$  left-hand extremity of  $s$
- 5:  $C' \leftarrow \{c \in C \setminus y_p - \epsilon \leq y_c \leq y_p + \epsilon\}$
- 6:  $c' \leftarrow \operatorname{argmax}_{c \in C'} \{|x_c - x_p|\}$
- 7: **if**  $C' \neq \emptyset$  and  $|x_{c'} - x_p| < \eta$  **then**
- 8: append  $s$  to  $c'$
- 9: **else**
- 10:  $c' \leftarrow$  new chain composed of  $s$
- 11: put  $c'$  in  $C$
- 12: **end if**
- 13:  $\text{Key}(c') \leftarrow y$ -coordinate of right-hand extremity of  $s$
- 14: **end for**

Fig. 6. Chaining process of basically horizontal segments.  $\epsilon$  and  $\eta$  are user-defined values controlling the accuracy of chaining.

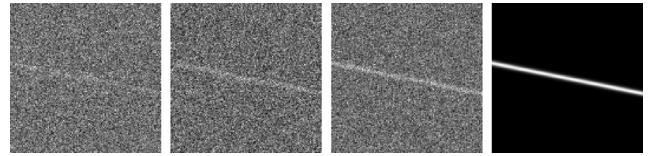


Fig. 7. Average maximum beamlet coefficient in function of scale, computed over a set of 100 simulated images at SNR =  $-5$ ,  $0$ , and  $5$  dB. Green bars correspond to FABT coefficients, blue bars correspond to BT coefficient and red dashed line stands for the ideal threshold.

structures of  $N$  elements requires  $\log_2(N)$  operations. Subsequently, the construction of the entire set of beamlet chains requires  $O(N \log_2(N))$  operations.

Once both *basically horizontal* and *vertical* sets of beamlet chains have been built, we merge them by looking for *basically horizontal* chains that have their extremities close enough to extremities of a *basically vertical* chain. Using the same data structure described as above, the overall complexity of that step is then equivalent to the previous steps complexity.

## IV. RESULTS

### A. Experiments on Simulated Images

In this section, we propose experiments on synthetic data demonstrating substantial improvements of the FABT over the classical Beamlet transform. These improvements concern both good detection performance and angular accuracy. To simulate images, we use the following parametric model: given a line segment  $(\sigma, x_c, y_c, \theta, L, A)$ , where  $\sigma$  is the vanishing width of the segment,  $(x_c, y_c)$  are the coordinates of the segment center,  $\theta$  is its angle with the  $x$ -axis,  $L = 2l$  the segment length, and  $A$  its mean intensity. Noise-free images are simulated using segment model proposed in [47] and defined as

$$f(x, y) = A \int_{-1}^1 g(x - x(t), y - y(t)) dt \quad (17)$$

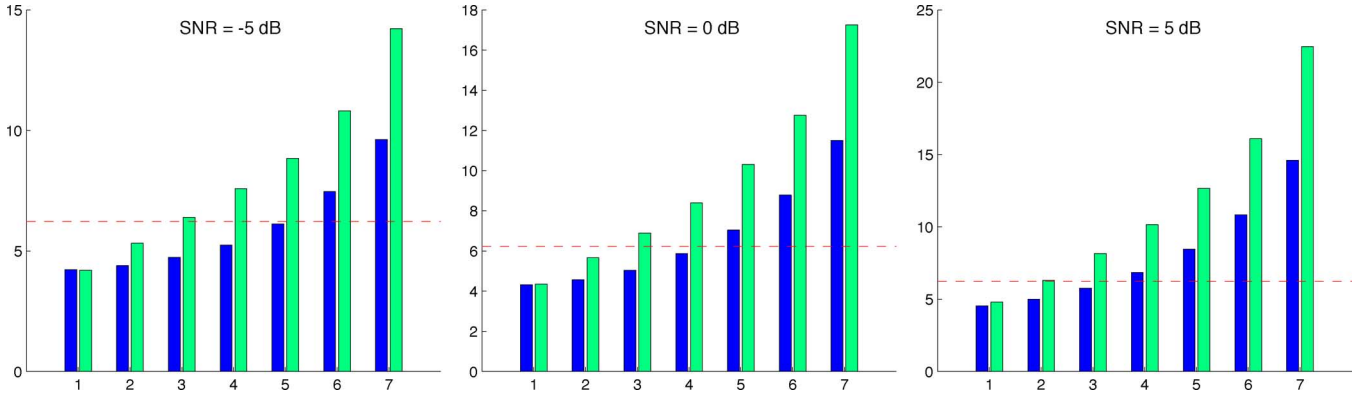


Fig. 8. Simulated images of a line feature corrupted by additive Gaussian noise of unit variance. Amplitude of the line feature is defined such as  $\text{SNR} = -10, 0, \text{ and } 10$  dB (from left to right). The right most image is noise free.

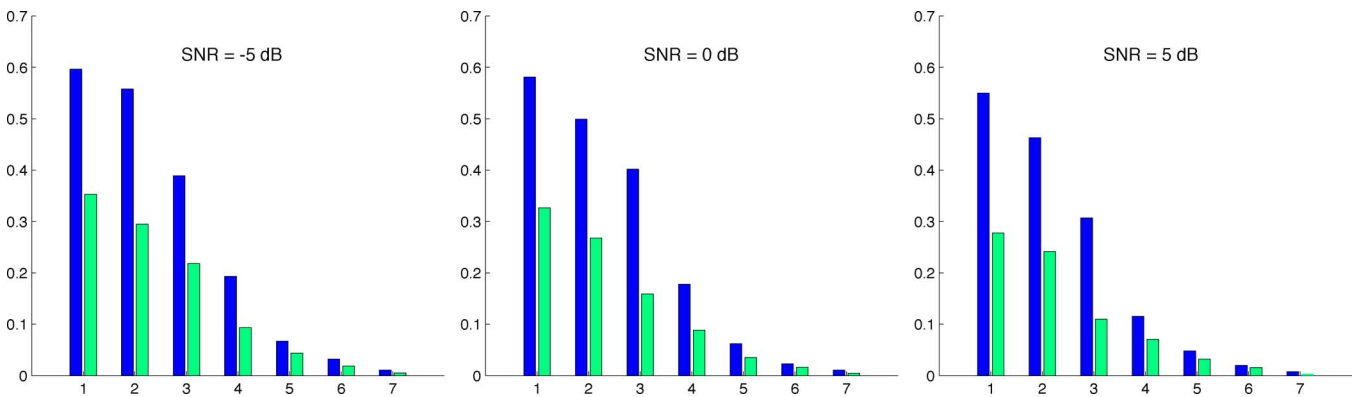


Fig. 9. Edge detection: (top-left) image corrupted by Gaussian white noise  $\sigma_{noise} = 50$ . (Top-right) Result of using the proposed method using a Canny edge filter and  $\alpha = 0.1\%$ . (Bottom) Results at the same statistical level for the Canny edge detector (left) and the third-order edge detector (right).

where  $x(t) = x_c + tl \cos(\theta)$  and  $y(t) = y_c + tl \sin(\theta)$  and  $g(x, y)$  is a Gaussian window of standard deviation  $\sigma$ . Additive Gaussian noise of null mean and unit variance is then added to produce images at various signal-to-noise ratio (SNR), defined here as  $\text{SNR} = 20 \log_{10}(A)$ . Examples images are shown in Fig. 7. Image size is  $128 \times 128$ .

In order to evaluate our feature-adapted beamlet transform (FABT) and to compare it to the classical Beamlet transform (BT), we proceed as follows: over a set of 100 simulated images at a given SNR, for each image 1) compute BT/FABT, 2) normalize beamlet coefficients, and 3) keep the maximum beamlet coefficient for each scale. For these experiments, a second-order ridge detector proposed in [35] has been used for filter  $h$ .

1) *Improving Good Detection Performance*: we compare, for each scale, the good detection performance, i.e., the intensity of coefficients for the BT and FABT. Fig. 8 displays the average maximum beamlet coefficient in function of scale at three different signal-to-noise ratios (from left to right,  $\text{SNR} = -5, 0, \text{ and } 5$  dB). For every scale, the average maximum FABT coefficient (green bars) is always greater than the BT coefficient (blue bars). When  $\text{SNR} = 0$  dB for example, taking the ideal threshold  $2\sqrt{\log_2(N)}$  as a reference (red dashed line), average maximum FABT coefficient at scale 3 and 4 are significant, while BT coefficients are not at same scales. This improvement is mainly due to the filtering step embedded into the FABT, enhancing the linear feature while reducing noise impact.

2) *Improving Angular Accuracy*: We evaluate, for each scale, the angular mean square error in radian between the maximum beamlet's orientation and the true orientation  $\theta$  of the line segment. Fig. 9 displays the angular error for BT (blue bars) and FABT coefficients (green bars) at  $\text{SNR} = -5, 0, \text{ and } 5$  dB (from left to right). As we can see, the angular error made by FABT is smaller than the one made by the BT. This behavior holds at each scale.

## B. Experiments on Real Data

1) *Edge Detection*: we test our method for edge detection on the classical "house" image and we compare the result with two different edge detectors, namely, the Canny edge detector and the third-order edge detector proposed in [35]. Fig. 10 shows results on a noisy image corrupted by Gaussian white noise with standard deviation  $\sigma_{noise} = 50$ . In our method, the Canny edge detector has been used for filter  $h$  and we set the statistical level  $\alpha = 0.1\%$ . We also use the well-known Bresenham algorithm to highlight pixels traversed by meaningful beamlets. For the 2 other edge detectors, we use a threshold value  $\tau = U_\alpha \|h\|_2 \sigma_{noise}$ , where  $U_\alpha$  is the Gaussian p-value for  $\alpha = 0.1\%$  and  $h$  stands for the Canny filter and the third-order edge filter, respectively. As expected, our method (top-right) is more robust to noise compared to the local edge detectors (bottom row). This is essentially due to the fact that the statistical tests are performed on segments of various lengths and not at the pixel level



Fig. 10. Angular mean square error (radian) between maximum beamlet's orientation and the true orientation  $\theta$  of the line segment, in function of scale, computed over a set of 100 simulated images SNR = -5, 0, and 5 dB. Green bars correspond to FABT angular error, blue bars correspond to BT angular error.

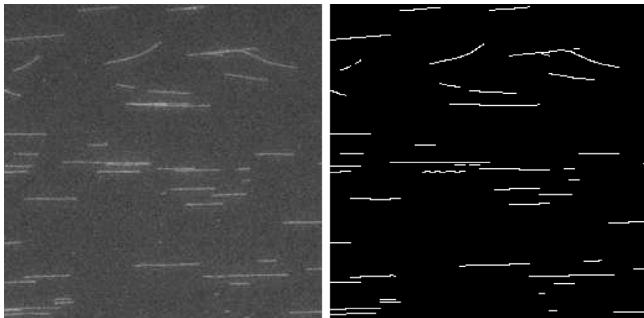


Fig. 11. Detection of  $\lambda$ -phage DNA molecules: original image (left), detection (right).

only. Our method is also able to retrieve features, for example most of the roof shadow lines, which are barely detected at pixel level, even though the filter used in our method (Canny) is less powerful than the third-order edge detector (bottom-right). Improved results could certainly be achieved by incorporating this third-order filter in our method.

2) *Ridge Detection*: an interesting domain of application, where the motivation of this work finds its origin, is the detection of filaments in fluorescent microscopy. In this framework, images can be very noisy and the detection of filament may be difficult. We test our method on the detection of two kinds of biological structures and we give some qualitative results.

A typical image of stretched DNA molecules of  $\lambda$ -phage is depicted in Fig. 11, where filaments are labelled and observed thanks to standard fluorescent microscopy. We can see that our methodology is adapted to detect linear structures as well as curvilinear ones. Moreover, even if filament intensity fluctuates along the filaments, being quite low at some points for instance, our method is able to fill these gaps.

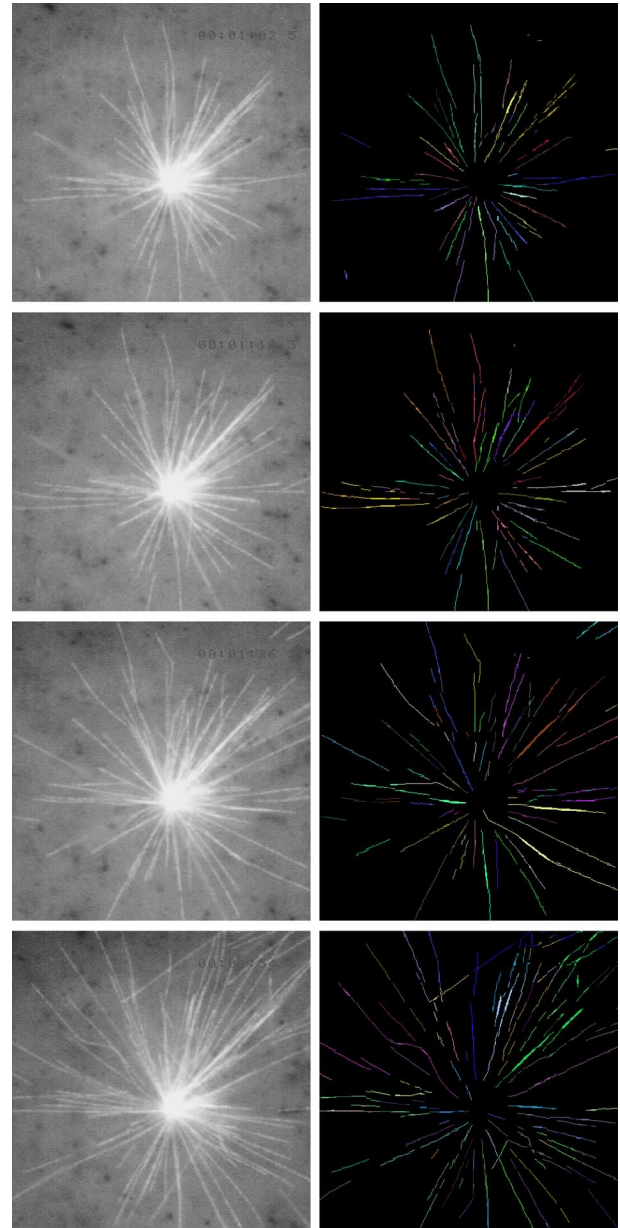


Fig. 12. Detection of full-length microtubules during interphase at  $t = 24$  s, 32, 48, and 76 s. Right column shows the detection after chaining step. Each filament is labeled by a single color.

We also test our detection method on a sequence of growing microtubules during interphase. The beamlet chaining step (algorithm 6) has been slightly modified in order to be adapted for microtubules images. As shown in Fig. 12, the centrosome, from which microtubules grow and shrink, is a huge bright spot for which location is easy to estimate. Then, thanks to that position, we convert beamlet coordinates into polar coordinate system before sorting beamlets, according to their radial coordinate. The rest of the algorithm is left unchanged. Each filament is labeled by a single color.

## V. DISCUSSION

In this paper, we have proposed a statistical detection framework for detecting features running along lines or piecewise

constant curves. This method relies on the feature-adapted beamlet transform (FABT). It allows to incorporate line profile information into the classical Beamlet transform introduced by Donoho *et al.* [23]. FABT is able to incorporate common image features like edges or ridges as well as any kind of 2-D features that can be designed by *a priori* knowledge. This new transform is achieved thanks to the combination of a multiscale dictionary, the beamlet set, and some linear feature detectors mechanisms. If the desired feature detector is chosen to belong to the class of steerable filters, the FABT only requires  $O(N \log(N))$  operations, where  $N = n^2$  is the number of pixels, and can be easily dispatched on a parallel machine.

We may notice that the proposed FABT, when  $h$  is chosen as a ridge detector, is very close to the multiscale ridgelet transform introduced by Candès [12]. Multiscale ridgelet is a pyramid of analyzing elements which consists of ridgelets transported to a wide range of dyadic scales and locations; each oriented element supports a ridge function in its transverse direction. However, some differences subsist; we point out that they mainly come from the fact that ridgelet transform has been designed for image representation and, therefore, will not be well suited for specific detection purposes. First, the central element to represent ridges in the ridgelet transform is achieved by wavelet decomposition; it provides a set of elements of different widths. This decomposition is not performed in the FABT since the width of element, for which the feature detector  $h$  is designed to detect, is fixed. We suggest that in case we have some *a priori* knowledge about the width of curvilinear objects we are looking for (for instance, this is mostly the case in biological images where objects have sub-resolutive width), this decomposition is not required. Moreover, the wavelet decomposition is dyadic and then, cannot optimally fit the object's width in a single scale. The second main difference between multiscale ridgelet transform and the FABT is the general shape of basis elements. The ridgelet transform applies a 1-D wavelet transform on Radon lines, which yields an atom which looks like a *tunnel* detector, with truncated extremities. In our case, a feature-adapted beamlet corresponds to a real segment detector, with smooth vanishing extremities along and across the ridge. This is due to the fact that our definition of features is already in 2-D. We suggest that this 2-D definition fits better to curvilinear objects found in real images.

In this paper, FABT has been embedded into a general framework for curvilinear objects detection with a statistical control over false detections. To satisfy that statistical demand, we propose a simple algorithm in four steps: 1) compute the FABT, 2) normalize beamlet coefficients, 3) select meaningful beamlets thanks to a fast energy-based minimization, and 4) put beamlets together in order to get a list of detected curves. We provide a validation of the proposed method on synthetic images as well as detection experiments on real data, demonstrating the substantial improvement of our method over classical feature detectors.

Based on the presented work, several improvements may be considered. For instance, we point out that the implementation of the Feature-adapted Radon transform could be improved and accelerated. In our current implementation, the number of pseudo-polar Fourier transforms that have to be performed depends on the number of basis filters composing filter  $h$ . If this

number is large, the overall process may be slow. As Fig. 2 has shown, each process around pseudo-polar Fourier transforms is a linear operation; if we make the analogy with classical Fourier transform and the use of the convolution theorem, these processes could be performed within a single pseudo-polar Fourier transform. Unfortunately, the convolution theorem does not hold for the pseudo-polar Fourier transform since it involves in one of the dimensions the fractional Fourier transform, for which the convolution theorem is not that simple. However, several works address that problem [26], [44] which should be further investigated.

Finally, we point out that the detection of filament junctions could certainly be improved. Like with many methods based on linear ridge filtering, junctions may not be well detected by our method and one branch of the junction is favored. Indeed, as can be seen in Fig. 12, the filtering step does yield partial detection of branches only, while one would expect that filament junctions be detected by a decomposition into many small squares (see Fig. 5). To overcome this limitation and properly detect branches, corners and crossings, one solution could be to use the multisteerable filters introduced in [39]. This will be investigated in future work.

#### APPENDIX A PROOF OF PROPOSITION 1

In order to prove Proposition 1, a detailed presentation of the pseudo-polar Fourier transform is needed. The pseudo-polar Fourier transform proceeds in two stages: It first computes the regular Fourier transform of the image on the cartesian grid  $((\pi/n)k_1, (\pi/n)k_2)$ , for  $-n \leq k_1, k_2 < n$ . Secondly, for each row  $k$ , it applies the following operator:

$$G_{n,k} = \frac{1}{m} \cdot \mathcal{F}_\alpha \circ \mathcal{F}_{-1}$$

where  $\mathcal{F}_\alpha$  is the 1-D fractional Fourier transform [5] with  $\alpha = 2k/n$ . This operator takes a series of  $2n$  values and provides  $n$  values which correspond to the  $k$ th row of the pseudo-polar Fourier transform (see [3] for complete details). Then, for a given angle  $\theta$ , we first compute the 2-D Fourier transform of  $I * h^\theta$

$$\widehat{I * h^\theta}(k_1, k_2) = \sum_{u,v} I * h^\theta(u, v) \exp \left\{ -i \frac{\pi}{n} (uk_1 + vk_2) \right\}$$

with  $-n \leq k_1, k_2 < n$ . We extract the  $k$ th row and apply  $G_{n,k}$ , which results in the following series of  $n$  numbers

$$\mathcal{F}_\alpha \left[ \mathcal{F}_1 [I * h^\theta(j, \cdot)] \left( \frac{\pi k}{n} \right) \right], \quad -n \leq j \leq n$$

where  $(j, \cdot)$  stands for the  $j$ th column and  $\mathcal{F}_1$  is the 1-D Fourier transform applied on columns. If  $h$  is selected to be within the class of steerable filters, we can rewrite the previous equation using (6)

$$\mathcal{F}_\alpha \left[ \mathcal{F}_1 \left[ \sum_{i=1}^M \phi_i(\theta) I * h^{\theta_i}(j, \cdot) \right] \left( \frac{\pi k}{n} \right) \right], \quad -n \leq j < n.$$

Due to the linearity of the operators  $\mathcal{F}_1$  and  $\mathcal{F}_\alpha$ , it yields to

$$\sum_{i=1}^M \phi_i(\theta) \underbrace{\mathcal{F}_\alpha \left[ \mathcal{F}_1 [I * h^{\theta_i}(\cdot, \cdot)] \left( \frac{\pi k}{n} \right) \right]}_{\mathcal{P}[I * h^{\theta_i}](\cdot, k)}, \quad -n \leq j < n.$$

where  $\mathcal{P}[I * h^{\theta_i}](\cdot, k)$  is the  $k$ th row of the pseudo-polar Fourier transform computed on  $I * h^{\theta_i}$ . This completes the proof.

#### APPENDIX B PROOF OF PROPOSITION 2

Using the property of linearity of Gaussian vectors, if an image  $I$  is a set of i.i.d. random variables following the normal distribution  $\mathcal{N}(\mu, \sigma^2)$ , we have

$$I * h^\theta \sim \mathcal{N}(\mu \|h\|_1, \sigma^2 \|h\|_2^2)$$

where  $\|h\|_1$  and  $\|h\|_2$  are respectively the  $L_1$ -norm and the  $L_2$ -norm of  $h$ . From [4], we have

$$\widetilde{I * h^\theta}(u, y) = \sum_{v=-n/2}^{n/2-1} I * h^\theta(u, v) D_m(y - v)$$

where  $D_m$  is a Dirichlet kernel defined as  $D_m(t) = \sin(\pi t)/m \sin(\pi t/m)$  with  $m = 2n + 1$ . Given  $X$  a

random vector defined as  $\begin{pmatrix} I * h^\theta(u, -n/2) \\ \vdots \\ I * h^\theta(u, n/2 - 1) \end{pmatrix}$  with

mean vector  $\bar{\mu} = \mu \|h\|_1 \begin{pmatrix} 1 \\ \vdots \\ 1 \end{pmatrix}$  and variance co-vari-

ance matrix  $\Sigma = \sigma^2 \|h\|_2^2 \begin{pmatrix} 1 & & \\ & \ddots & \\ & & 1 \end{pmatrix}$ , we define

$\widetilde{I * h^\theta}(u, y)$  as a random variable  $Y = AX$ , where

$A = \begin{pmatrix} D_m(y - (-n/2)) \\ \vdots \\ D_m(y - (n/2 - 1)) \end{pmatrix}^T$ .  $Y$  is following a normal

distribution of mean  $\bar{\mu}A$  and variance  $A\Sigma A^{-1}$ . Consequently

$$\widetilde{I * h^\theta}(u, y) \sim \mathcal{N} \left( \mu \|h\|_1 \sum_{v=-n/2}^{n/2-1} D_m(y - v), \sigma^2 \|h\|_2^2 \sum_{v=-n/2}^{n/2-1} D_m(y - v)^2 \right). \quad (18)$$

Applying the same reasoning on  $\mathcal{R}[I * h^\theta](\theta, t)$ , we deduce

$$\mathcal{R}[I * h^\theta](\theta, t) \sim \mathcal{N}(\mu_{\mathcal{R}}, \sigma_{\mathcal{R}}^2)$$

with

$$\begin{aligned} \mu_{\mathcal{R}} &= \mu \|h\|_1 \sum_{u=-n/2}^{n/2-1} \sum_{v=-n/2}^{n/2-1} D_m(\tan(\theta)u + t - v) \\ &= \mu \|h\|_1 \sum_{u=-n/2}^{n/2-1} \sum_{v=-n/2}^{n/2-1} \mathbf{1}(u, v) (D_m(\tan(\theta)u + t - v)) \\ &= \mu \|h\|_1 \sum_{u=-n/2}^{n/2-1} \tilde{\mathbf{1}}(u, \tan(\theta)u + t) \\ &= \mu \|h\|_1 \mathcal{R}[\mathbf{1}](\theta, t) \end{aligned}$$

where  $\mathbf{1}(u, v)$  equals to 1 for every  $(u, v)$  and

$$\sigma_{\mathcal{R}}^2 = \sigma^2 \|h\|_2^2 \sum_{u=-n/2}^{n/2-1} \sum_{v=-n/2}^{n/2-1} D_m(\tan(\theta)u + t - v)^2.$$

#### REFERENCES

- [1] E. Arias-Castro, D. Donoho, and X. Huo, "Adaptive multiscale detection of filamentary structures in a background of uniform random points," *Ann. Statist.*, vol. 34, no. 1, pp. 326–349, 2006.
- [2] E. Arias-Castro, D. Donoho, and X. Huo, "Near-optimal detection of geometric objects by fast multiscale methods," *IEEE Trans. Inf. Theory*, vol. 51, no. 7, pp. 2402–2425, Jul. 2005.
- [3] A. Averbuch, R. Coifman, D. Donoho, M. Israeli, Y. Shkolnisky, and I. Sedelnikov, "A framework for discrete integral transformations I – The pseudo-polar Fourier transforms," *SIAM J. Sci. Comput.*, vol. 30, no. 2, 2008.
- [4] A. Averbuch, R. Coifman, D. Donoho, M. Israeli, Y. Shkolnisky, and I. Sedelnikov, "A framework for discrete integral transformations II – The 2D discrete Radon transforms," *SIAM J. Sci. Comput.*, vol. 30, no. 2, 2008.
- [5] D. H. Bailey and P. N. Swartztrauber, "The fractional Fourier transform and applications," *SIAM Rev.*, vol. 33, no. 3, pp. 389–404, 1995.
- [6] S. Berlemont, A. Bensimon, and J.-C. Olivo-Marin, "Detection of curvilinear objects in biological noisy image using feature-adapted fast slant stack," presented at the SPIE Conf. Wavelets XII, Special Session on Wavelet in Bioimaging, Aug. 2007.
- [7] S. Berlemont, A. Bensimon, and J.-C. Olivo-Marin, "Detection of curvilinear objects in noisy image using feature-adapted beamlet transform," presented at the IEEE Int. Conf. Acoustic, Speech and Signal Processing, Apr. 2007.
- [8] J. Bobin, J. Bobin, J.-L. Starck, J. Fadili, and Y. Moudden, "Sparsity and morphological diversity in blind source separation," *IEEE Trans. Image Process.*, vol. 16, pp. 2662–2674, 2007.
- [9] A. Brandt and J. Dym, "Fast calculation of multiple line integrals," *SIAM J. Sci. Comput.*, vol. 20, no. 4, pp. 1417–1429, 1999.
- [10] E. Candès, "Ridgelets: Theory and Applications," Ph.D. dissertation, Dept. Statist., Stanford Univ., Stanford, CA, 1998.
- [11] E. Candès and D. Donoho, "Curvelets – A Surprisingly Effective Non-adaptive Representation of Objects with Edges," Tech. Rep. California Inst. Technol., Pasadena, 1999.
- [12] E. Candès and D. Donoho, "Recovering edges in ill-posed inverse problems: Optimality of curvelet frames," *Ann. Statist.*, vol. 30, no. 3, pp. 784–842, 2002.
- [13] E. Candès and D. Donoho, "New tight frames of curvelets and optimal representations of objects with piecewise c[2] singularities," *Commun. Pure Appl. Math.*, vol. 57, no. 2, pp. 219–266, 2004.
- [14] J. Canny, "A computational approach to edge detection," *IEEE Trans. Pattern Anal. Mach. Intell.*, vol. PAMI-8, no. 6, pp. 679–698, Jun. 1986.
- [15] T. H. Cormen, C. E. Leiserson, and R. L. Rivest, *Introduction to Algorithms*. Cambridge, MA: MIT Press, 1990.
- [16] I. J. Cox, J. M. Rehg, and S. Hingorani, "A bayesian multiple-hypothesis approach to edge grouping and contour segmentation," *Int. J. Comput. Vis.*, vol. 11, no. 1, pp. 5–24, 1993.

- [17] I. Daubechies, *Ten Lectures on Wavelets*. Philadelphia, PA: SIAM, 1992.
- [18] M. Do and M. Vetterli, "Orthonormal finite ridgelet transform for image compression," in *Proc. IEEE Int. Conf. Image Processing*, Sep. 10–13, 2000, vol. 2, pp. 367–370.
- [19] M. Do and M. Vetterli, "The finite ridgelet transform for image representation," *IEEE Trans. Image Process.*, vol. 12, pp. 16–28, 2003.
- [20] M. Do and M. Vetterli, "The contourlet transform: An efficient directional multiresolution image representation," *IEEE Trans. Image Process.*, vol. 14, pp. 2091–2106, 2005.
- [21] D. L. Donoho, "Wedgelets: Near minmax estimation of edges," *Ann. Statist.*, vol. 27, no. 3, pp. 859–897, 1999.
- [22] D. L. Donoho and X. Huo, "Beamlet pyramids: A new form of multiresolution analysis, suited for extracting lines, curves, and objects from very noisy image data," in *Proc. SPIE*, 2000, vol. 4119, pp. 434–444.
- [23] D. L. Donoho and X. Huo, "Beamlets and multiscale image analysis," in *Proc. Multiscale and Multiresolution Methods*, 2001, vol. 20, pp. 149–196, Lecture Notes in Computational Science and Engineering.
- [24] D. L. Donoho and O. Levi, "Fast x-ray and beamlet transforms for three-dimensional data," in *Modern Signal Processing*, D. N. Rockmore and D. M. Healy, Jr., Eds. Cambridge, U.K.: Cambridge Univ. Press, 2002, vol. 46, pp. 79–116.
- [25] D. Eberly, R. Gardner, B. Morse, S. Pizer, and C. Scharlach, "Ridges for image analysis," *J. Math. Imag. Vis.*, vol. 4, no. 4, pp. 353–373, 1994.
- [26] T. Erseghe, P. Kraniuskas, and G. Carioraro, "Unified fractional Fourier transform and sampling theorem," *IEEE Trans. Signal Process.*, vol. 47, no. 12, pp. 3419–3423, Dec. 1999.
- [27] W. T. Freeman and E. H. Adelson, "The design and use of steerable filters," *IEEE Trans. Pattern Anal. Mach. Intell.*, vol. 13, no. 9, pp. 891–906, Sep. 1991.
- [28] Y. Huang, I. Pollak, M. Do, and C. Bouman, "Fast search for best representations in multitree dictionaries," *IEEE Trans. Image Process.*, vol. 15, no. 7, pp. 1779–1793, Jul. 2006.
- [29] P. J. Huber, *Robust Statistics*. Hoboken, NJ: Wiley, 1981, Wiley Series in Probability and Statistics.
- [30] X. Huo and D. Donoho, "Recovering filamentary objects in severely degraded binary images using beamlet-driven partitioning," in *Proc. IEEE Int. Conf. Acoustics, Speech, and Signal Processing*, Dec. 2002, vol. 2, pp. 1265–1268.
- [31] X. Huo, "Exact lower bound for proportion of maximally embedded beamlet," *J. Appl. Math. Lett.*, vol. 18, no. 5, pp. 529–534, 2005.
- [32] X. Huo, "Minimax correlation between a line segment and a beamlet," *Statist. Probab. Lett.*, vol. 72, no. 1, pp. 71–81, 2005.
- [33] X. Huo, J. Chen, and D. L. Donoho, "Multiscale detection of filamentary features in image data," in *Proc. SPIE Conf. Wavelets X: Applications in Signal and Image Processing*, 2003, vol. 5207, pp. 592–606.
- [34] X. Huo and Y. Jihong Cheng, "Jbeam: Multiscale curve coding via beamlets," *IEEE Trans. Image Process.*, vol. 14, no. 11, pp. 1665–1677, Nov. 2005.
- [35] M. Jacob and M. Unser, "Design of steerable filters for feature detection using Canny-like criteria," *IEEE Trans. Pattern Anal. Mach. Intell.*, vol. 26, no. 8, pp. 1007–1019, Aug. 2004.
- [36] E. Le Pennec and S. Mallat, "Sparse geometric image representations with bandelets," *IEEE Trans. Image Process.*, vol. 14, no. 4, pp. 423–438, Apr. 2005.
- [37] S. Mallat, "A theory for multiresolution signal decomposition: The wavelet representation," *IEEE Trans. Pattern Anal. Mach. Intell.*, vol. 11, no. 7, pp. 674–693, Jul. 1989.
- [38] S. Mallat, *A Wavelet Tour of Signal Processing*, 2nd ed. New York: Academic, 1999.
- [39] M. Mühlich, T. Dahmen, and T. Aach, "Design of multi-steerable filters and their application for the detection of corners and junctions," in *Proc. IEEE Int. Conf. Image Processing*, 2007, vol. 4, pp. IV – 33–IV – 36.
- [40] J.-L. Starck, F. D. Murtagh, and A. Bijaoui, *Image Processing and Data Analysis. The Multiscale Approach*, 1st ed. Cambridge, U.K.: Cambridge Univ. Press, 1998.
- [41] J. Starck, E. Candès, and D. Donoho, "The curvelet transform for image denoising," *IEEE Trans. Image Process.*, vol. 11, no. 6, pp. 670–786, Jun. 2002.
- [42] J. Starck, V. Martinez, D. Donoho, O. Levi, P. Querre, and E. Saar, "Analysis of the spatial distribution of galaxies by multiscale methods," *EURASIP J. Appl. Signal Process.*, vol. 15, pp. 2455–2469, 2005.
- [43] V. Velisavljevic, B. Beferull-Lozano, M. Vetterli, and P. L. Dragotti, "Directionlets: Anisotropic multidirectional representation with separable filtering," *IEEE Trans. Image Process.*, vol. 15, no. 7, pp. 1916–1933, Jul. 2006.
- [44] A. Zayed, "A convolution and product theorem for the fractional Fourier transform," *IEEE Signal Process. Lett.*, vol. 5, no. 4, pp. 101–103, Apr. 1998.
- [45] B. Zhang, J. Fadili, and J.-L. Starck, "Wavelets, ridgelets and curvelets for Poisson noise removal," *IEEE Trans. Image Process.*, vol. 17, no. 7, pp. 1093–1108, Jul. 2008.
- [46] B. Zhang, J. Zerubia, and J.-C. Olivo-Marin, "Gaussian approximations of fluorescence microscope PSF models," *J. Appl. Opt.*, vol. 46, no. 10, pp. 1819–1829, 2006.
- [47] B. Zhang, J. Enninga, J.-C. Olivo-Marin, and C. Zimmer, "Automated super-resolution detection of fluorescent rods in 2d," in *Proc. IEEE Int. Symp. Biomedical Imaging: Macro to Nano*, Apr. 6–9, 2006, pp. 1296–1299.



**Sylvain Berlemont** (S'05) received the B.S. degree in computer science and the M.S. degree in image processing and computer vision from the Université Pierre et Marie Curie, Paris, France, in 2003 and 2004, respectively, and the Ph.D. degree in biomedical image analysis from the Institut Pasteur, Paris, in 2008.

He is now a postdoctoral Fellow in the Department of Cell Biology, Harvard Medical School, under the guidance of Prof. Danuser. His research interests is to push forward the development of data modeling and image analysis approaches to gain quantitative understanding of cell biological mechanisms.



**Jean-Christophe Olivo-Marin** (M'93–SM'05) received the Ph.D. degree and the "Habilitation à Diriger des Recherches" from the Institut d'Optique Théorique et Appliquée, University of Paris-Orsay, France, in 1989 and 1998, respectively.

He is Head of the Quantitative Image Analysis Unit at the Institut Pasteur. He was a co-founder of the Institut Pasteur Korea, Seoul, where he held a joint appointment as Chief Technology Officer from 2004 to 2005. Previous to that, he was a staff scientist from 1990 to 1998 at the European Molecular Biology Laboratory, Heidelberg, Germany. He has a long experience of multidisciplinary approaches in biological imaging and his research interests are in the image analysis of multidimensional microscopy images, pattern recognition, and motion analysis for cellular dynamics studies.

Dr. Olivo-Martin is a member of the SPS and EMBS, Chair of the Bio Imaging and Signal Processing Technical Committee (BISP-TC), the Pattern Recognition Society, and a member of the Editorial Board of the journal *Medical Image Analysis*. He has organized several special sessions dedicated to biological imaging at international biomedical conferences (ELMI'02, ELISO'03, ISBI'04, ICASSP'06, and SPIE Wavelets'09) and was General Chair of the IEEE International Symposium on Biomedical Imaging held in Paris in 2008.